A Multiscale X-Ray Tomography Study of the Cycled-Induced Degradation in Magnesium–Sulfur Batteries

Wenjia Du, Zhangxiang Hao, Francesco Iacoviello, Lin Sheng, Shaoliang Guan, Zhenyu Zhang, Daniel J. L. Brett, Feng Ryan Wang,* and Paul R. Shearing*

Rechargeable Mg/S batteries have the potential to provide a compelling battery for a range of applications owing to their high capacity and gravimetric energy density, safety, and low-cost construction. However, the Mg/S energy storage is not widely developed and deployed due to technical challenges, which include short cycle lifespan and lack of suitable electrolyte. To study the microstructure degradation of Mg/S batteries, multiscale X-ray tomography, an inherently nondestructive method, is performed on dismantled Swagelok Mg/S cells comprising a graphene–sulfur cathode and a super-P separator. For the first time, 3D microstructure visualization and quantification reveal the dissolution (volume fraction decreases from 13.5% to 0.7%, surface area reduces from 2.91 to 1.74 μm^2 μm^{-3}) and agglomeration of sulfur particles, and the carbon binder densification after 10 cycles. Using tomography data, the image-based simulations are then performed. The results show that the insoluble polysulfides can inevitably block the Mg^{2+} transportation via shuttle effect. The representative volume should exceed 8200 μm^3 to represent bulk cathode. This work elucidates that the Mg/S cell performance is significantly affected by microstructural degradation, and moreover demonstrates how multiscale and multimodal characterization can play an indispensable role in developing and optimizing the Mg/S electrode design.

1. Introduction

The rechargeable lithium–sulfur (Li/S) battery has been widely studied due to its superior theoretical energy density (2600 Wh Kg^{-1}), which is nearly 4–5 times higher than lithium-ion batteries (LIBs).[1] Although the electrochemical performance of Li/S has significantly improved,[2] the growth of mossy lithium dendrites at the anode during discharge is an ongoing challenge.

As an alternative battery chemistry, the concept of a rechargeable magnesium–sulfur (Mg/S) battery was proposed by Toyota Motor Corp. in 2011,[3] which can demonstrate the following advantages: 1) improved safety because Mg does not form dendrites, 2) lower cost due to the abundance of both magnesium and sulfur (as the raw materials for electrodes), and 3) the reaction: $Mg^{2+} + S + 2e^- \leftrightarrow MgS$ provides higher theoretical volumetric capacity (3833 mAh cm^{-3}).[4] Such two electron processes yield a theoretical voltage of 1.77 V, making the Mg/S theoretical energy density 3221 Wh L^{-1} (higher than 2856 Wh L^{-1} of Li/S).[5] The current limitations are 1) both the elemental sulfur and the associated discharged products of Mg/S are intrinsically electrically insulating. The poor electrochemical behavior is attributed to the low sulfur utilization and the formation of insoluble magnesium polysulfides and 2) the limited availability of a suitable electrolyte: a non-nucleophilic electrolyte is usually required to achieve sufficiently high ionic conductivity.[6]

Recently, improved lifespan and safer cells have been demonstrated through the significant development of the cathode,

Dr. W. Du, Dr. F. Iacoviello, Dr. Z. Zhang, Prof. D. J. L. Brett, Prof. P. R. Shearing
Electrochemical Innovation Lab
Department of Chemical Engineering
University College London
London WC1E 7JE, UK
E-mail: p.shearing@ucl.ac.uk
Dr. Z. Hao, L. Sheng, Dr. F. R. Wang
Materials and Catalysis Laboratory
Department of Chemical Engineering
University College London
London WC1E 7JE, UK
E-mail: ryan.wang@ucl.ac.uk

The ORCID identification number(s) for the author(s) of this article can be found under https://doi.org/10.1002/smtd.202001193.

Dr. S. Guan
HarwellXPS
Research Complex at Harwell
Rutherford Appleton Laboratory
Didcot OX11 0FA, UK
Dr. S. Guan
School of Chemistry
Cardiff University
Cardiff CF10 3AT, UK
Dr. Z. Zhang, Prof. D. J. L. Brett, Prof. P. R. Shearing
The Faraday Institution
Quad One
Harwell Science and Innovation Campus
Didcot OX11 0RA, UK

ADVANCED
SCIENCE NEWS
www.advancedsciencenews.com

small
methods
www.small-methods.com

separator and electrolyte. For example, Zhao-Karger et al.[7] developed a $Mg[B(hfip)_4]_2$ electrolyte to obtain excellent long-term Mg cycling stability with a low polarization. Du et al.[8] developed an advanced cathode (SeS_2/CMK3, SeS_2 composite with ordered mesoporous carbon) with a Cu foam interlayer between cathode and separator, which has an excellent electrochemical performance. Yin et al.[9] developed a functional interlayer separator for Li/S batteries which not only intercepts dissolved lithium polysulfides (mitigating the shuttle effect) but also acts as a reservoir to accommodate lithium polysulfides during cycling (buffering the dramatic volume change). Vinayan et al.[10] employed operando Raman spectroscopy to study polysulfide formation and chemical transformation. Sheng et al.[11] developed a performance-safety-cost map for Mg–S electrolyte via correlating the thermal runaway tests. However, the development of Mg/S battery studies is still in the early stage, and the microstructure-related degradation is yet to be rationalized.

The recent advancement of nondestructive X-ray imaging techniques (both using laboratory and synchrotron sources) has enabled researchers to characterize electrodes for energy storage at multiple length and time scales.[12] Particularly, X-ray computed tomography (X-ray CT) has been used to reveal 3D microstructure of a wide range of batteries. For example, Lu et al.[13]

used nano-CT to reveal how the elongated shape of active particles affects the lithium transport and current distribution under high rate conditions, to optimize the design of LIBs. Tan et al. used synchrotron X-ray tomography to reveal the fundamental Li/S cell mechanism by studying the sulfur dissolution and redeposition during cycling.[14] Although a similar phase transformation mechanism at the cathode might be expected in the Mg/S system, to date, there remains no report in such system.

In this study, we have developed a high-performance Mg/S cell (the discharge reversible capacity achieved 772 mAh g^{-1} in the 1st cycle) comprising a graphene–sulfur composite cathode, a super-P coated separator, electrolyte and a Mg anode which we have used for multiscale imaging. For the first time, we have combined scanning electron microscopy (SEM), energy-dispersive X-ray spectroscopy (EDX), X-ray photoelectron spectroscopy (XPS), and micro- and nanoscale X-ray tomography (micro-/nano-CT) techniques to investigate cycled-induced degradation for Mg/S cells (**Figure 1**). We explored the potential Mg/S degradation mechanism through 3D visualization, quantification, and image-based simulation, all correlated with electrochemical measurements. Our results show that, at the cathode, the sulfur dissolution and porosity agglomeration are mainly responsible
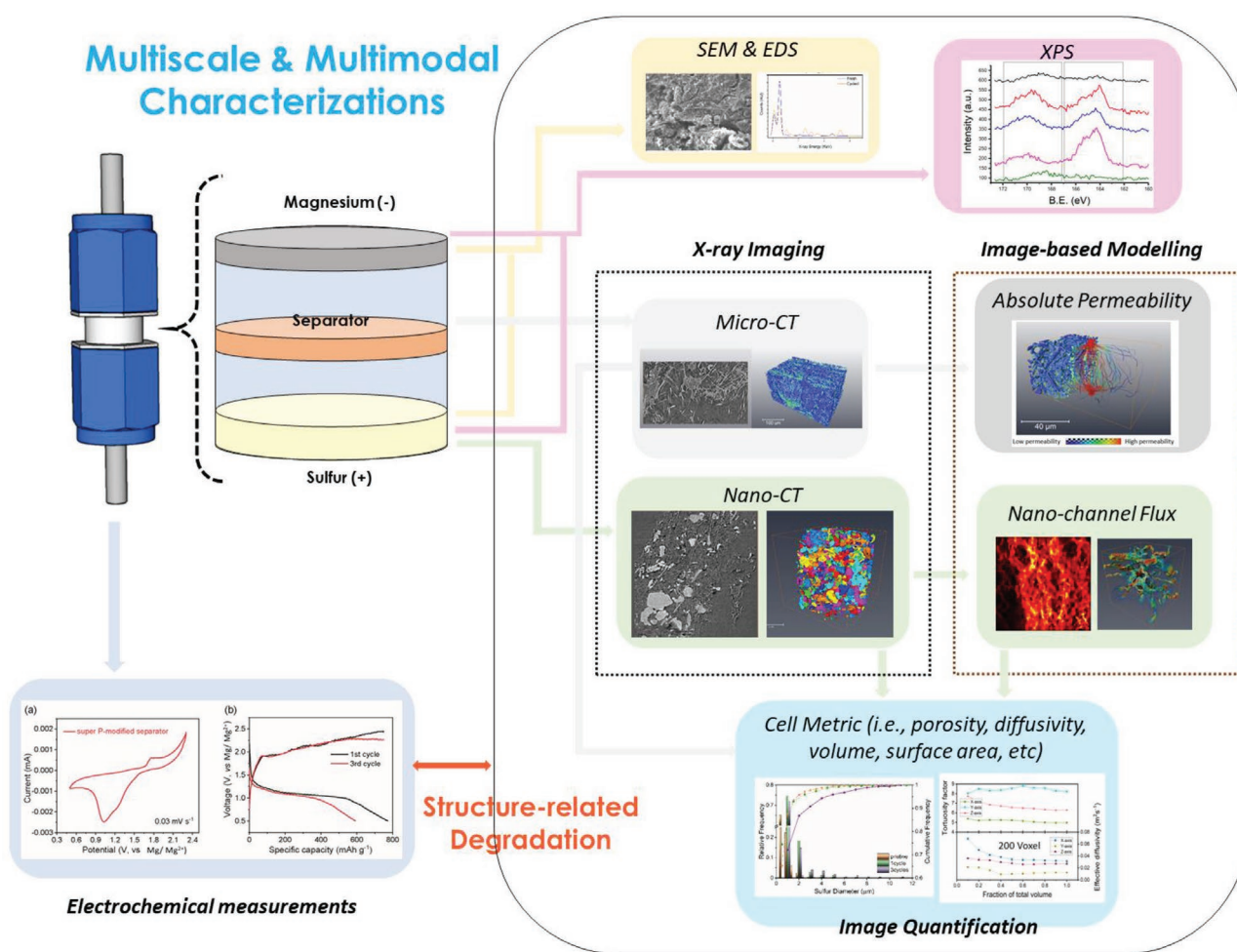

Figure 1. Schematic illustrates the multiscale and multimodal analysis workflow of rechargeable magnesium–sulfur cell. The anode was characterized by SEM and XPS, the super-P separator was performed with micro-CT, and the S/C cathode disk was illuminated by using a combination of SEM, XPS, and nano-CT. Finally, the image-based modeling was performed by employing the Avizo XLab (for separator) and TauFactor (for cathode), respectively.

for the reduction of cell lifespan. The volume fraction of S particles significantly decreased from 13.5% to 0.7% after 10th cycles. Following the 1st cycle, the separator experienced lower mass transportation because of the blockage by those insoluble polysulfides, confirmed by image-based simulation.

2. Results and Discussion

2.1. Multiscale and Multimodal Characterization of Electrodes Morphology, Structure, and Chemistry

SEM images of the anode and cathode were obtained to study the cycle-induced electrode morphologies. Mg sam-

ples were prepared 1–2 h prior to the SEM characterization and stored within the vials in Ar-filled environment, to minimize air exposure, however the Mg sample surface might be still affected. On the cathode side (column 1–2 of **Figure 2**), microcracks were obviously observed in porous sample after the 3rd and 10th cycles (Figure 2d,e). The size of crack increased with cycle number. These cracks may be attributed to volume change since the Mg/S cell involves solid–liquid–solid phase transformation during cycling. The peak intensity of sulfur gradually decreases and eventually disappears after 3 cycles (column 2 of Figure 2). Elemental Mg, aluminum (Al), and chlorine (Cl) were identified at the cathode surface (Figure 2g–j) that are originated from the electrolyte. The detection of both Mg and S at the cathode surface also
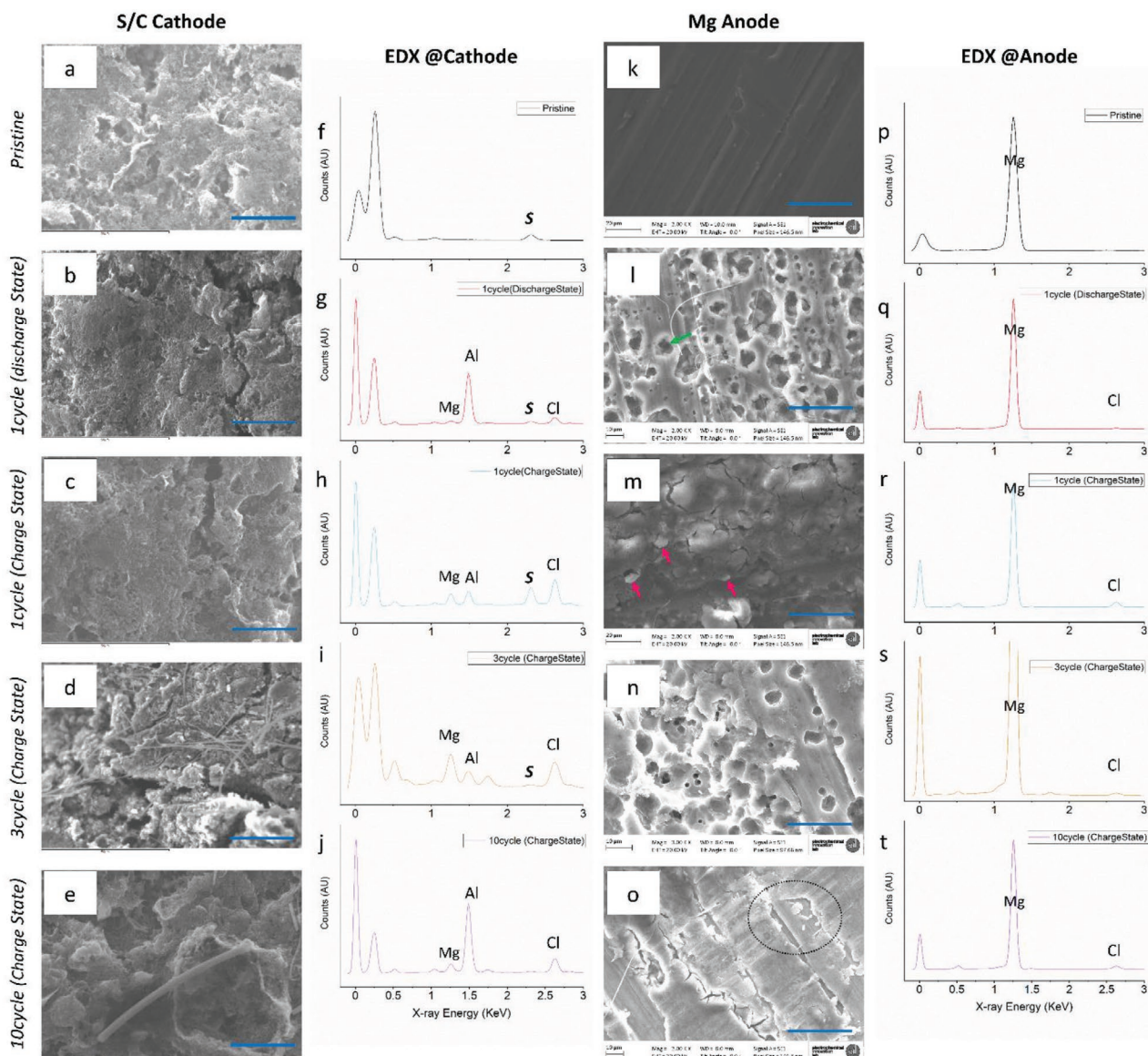

Figure 2. Scanning electron images cross-sections of a–e, column 1) the carbon–sulfur composite cathodes and k–o, column 3) the Mg metal anode at pristine and after 1st, 3rd, and 10th cycles in magnesium–sulfur (Mg/S) batteries taken at magnification of 3 K. The micro- and nanoscale cracks are clearly observed after cycle at S/C cathodes. The associated EDX spectra (up to 3 keV) of the pristine and cycled of (f–j, column 2) the S/C cathode and p–t, column 4) the Mg anode. The small pits (stripping) and depositions (plating) are observed at anode side. The appearance of elemental Mg at cathode suggests it is possible to produce the magnesium polysulfide via the similar mechanism in Li/S battery.

2001193 (3 of 13)

indicates it is possible to generate the magnesium polysulfides (MgS_x) after cycling. Insoluble polysulfides have been previously reported in alkaline–sulfur batteries.[15] On the anode side (column 3–4 of Figure 2), no obvious features on the planar surface (Figure 2a) were found in the pristine sample. Unlike Li, Mg dendrite formation during deposition/stripping was not observed. Instead, we found a large number of small pits (green arrow) and sub-pits with different diameters (up to ≈20 µm) on the Mg surface after 1st (Figure 2l) and 3rd (Figure 2n) cycle at charge-state, indicating nonuniform Mg^{2+} stripping. However, after the 10th cycle, the charged-state sample did not show similar pit-like features. Instead, the surface was covered by a thin layer (black dot circle). Also, the depositions included ridge-like structure, (red arrow) and microcracks (length of 5–10 µm), which were observed in 1st cyclic discharge-state sample (Figure 2m). Elemental Cl and Mg were identified after cycling via EDX spectra (column 4 of Figure 2), and they are stemmed from the electrolyte (containing $MgCl_2$), together with small amount of the oxygen (O). Our anodic SEMs are comparable with AFM investigation of Hu et al.[16]

To further understand the electrode chemistry against different cycle life, both the cathode (**Figure 3**) and anode (Figure S1, Supporting Information) of the Mg/S cell were investigated by X-ray photoelectron spectroscopy (XPS). For the pristine cathode, the S peak intensity at 164 eV is not strong, because the sulfur particles may impregnate deeper into the

carbon matrix (penetration depth of XPS is less than 10 nm). Indeed, interior nano-CT helps to reveal the sulfur particles in 3D. However, S $2p_{3/2}$ and S $2p_{1/2}$ peaks at 164.0 and 165.2 eV are subsequently resolved in the 1st and 3rd cycled cathode, which are assigned to element sulfur.[10,17] The formation of MgS usually at 161 eV according to Zhao-Karger et al.,[7] while in our discharge sample we are unable to see peak at this bond energy. This is attributed to all samples have been washed by solvent (tetraethylene glycol dimethyl ether, TEGDME). There are no S $2p_{3/2}$ and/or S $2p_{1/2}$ peaks in 10th cycled cathode (green line), as the sulfur was considerably consumed. This is confirmed by EDX mapping and nano-CT observation. The cathode signals increase at around 170 eV and suggests that the sulfur deposits over carbon/graphene layer and the formation of S−O bond. Nevertheless, doublet S spectra in Figure 3 indicate the good sulfur reversibility of Mg/S cell within 3 cycles.

Although SEM, EDX, and XPS provide some useful information (i.e., elemental distribution), they are intrinsically limited to 2D surficial investigations. Therefore, based on the information learnt from SEM images, a series of X-ray CT measurements (3D investigations) were selectively performed to complement the understanding of cycle-induced materials degradation of Mg/S batteries at multiple dimensions.

We first used micro-CT to study the super-P functional separator (**Figure 4**; Movie S1, Supporting Information). The cross-sectional slices show that the brighter phase is glassy fiber and the peripheral darker phase can be either air or carbon or both phases (Figure 4a). After cycling, in Figure 4d we clearly observed that an additional phase (light gray) was deposited on the surface of the glassy fibers. Considering the separator is an inert material which cannot react with any other materials within cell, the deposits are assumed to be either short-chain MgS_x or MgS or both. During the discharge process, the successive reduction in S generates magnesium polysulfides (MgS_x, $x = 1$–8) with various chain lengths, and the amorphous MgS_x polysulfides could diffuse between the S/C cathode and the Mg anode.[18] But the end-products (MgS_2 and MgS) are insoluble in the electrolyte and are redistributed on the conductive scaffolds which could be detected by X-ray tomography. The charge reaction is generally reversed from discharge.[5,19] Furthermore, the deep discharge products (MgS) in the cathode are difficult to completely dissolve during the charge process, therefore the phase transition is not completed. Indeed, our observation from X-ray CT confirmed the speculations, because the functional separator accommodated a small amount of deposited polysulfides ($V_{f\text{-deposition}} = 13\%$), which may mitigate the risk of volume changes. This buffer effect could be useful, particularly as the volume change is more noticeable in a pouch cell geometry. The 3D microstructures of functional separator are displayed, showing the fiber (blue) without and with the insoluble deposition (green) at the fresh (Figure 4b) and cycled (Figure 4e) state.

Table 1 summarizes values including phase volume fraction (V_f) and specific surface area (S_{Area}). Although two different samples are used, the $V_{f\text{-fibers}}$ showed very similar values (≈14%) before and after cycling. These products are preferably deposited at the intersection of glassy fibers (Figure 4d). The denser the fibers, the greater the amount of deposition, as they become trapped at junctions between fibers since the polysulfides (i.e., MgS) could stay within the separator (Figure 3b). To study to what extent
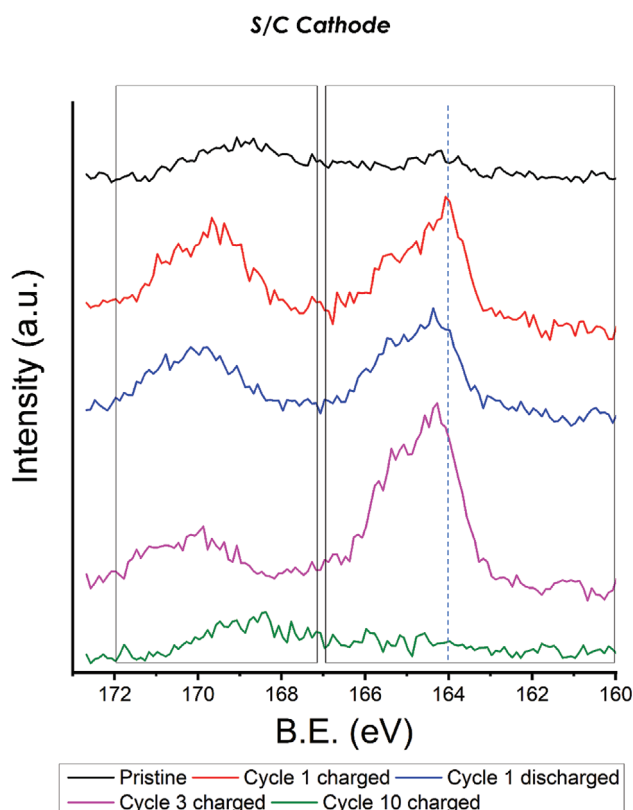
S/C Cathode

Figure 3. The high-resolution XPS shows S 2p spectra of the S/C cathodes at pristine and after 1st (in both charge and discharge state), 3rd, and 10th cycle.
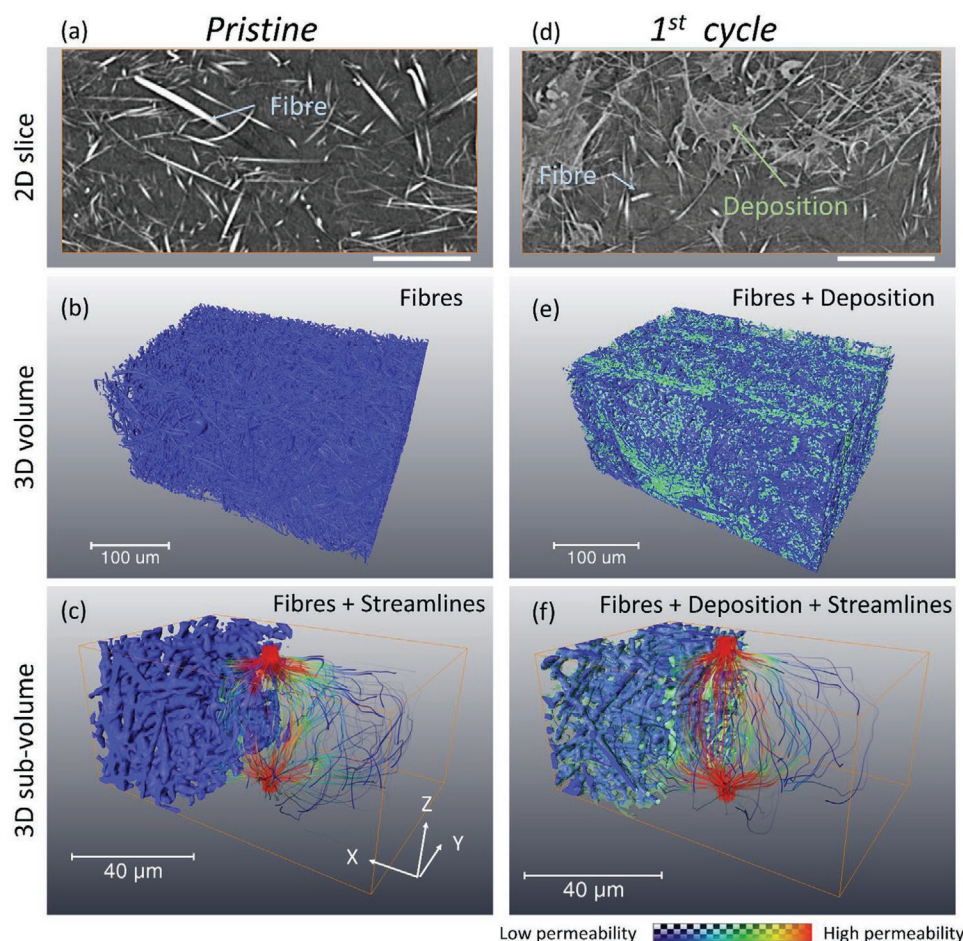
ADVANCED
SCIENCE NEWS

www.advancedsciencenews.com

small
methods

www.small-methods.com

Figure 4. The X-ray micro-CT images of a–c) the pristine and d–f) the 1st cycles super-P separator interlayer in the Mg/S battery. The extracted cross-sectional slices in the *X*–*Z* plane (a,d) show the low-chain polysulfides (X-ray attenuation depicted through a grayscale) could deposit and remain within the separator after 1st cycle. The associated 3D volume renderings of c) the pristine and f) the 1st cycled super-P separator samples show distribution of magnesium polysulfides (malachite green) in whole sample, providing the evidence of phase transformation in Mg/S batteries. The imaged-based simulation of flow permeabilities without (c) and with the deposit phases (f) in the subvolume extracted from the entire volume in (b) and (e) at the *Z*-axis direction. The associated quantifications are in Tables 1 and 2. (a,b) Scale bars represent 100 μm.

these products hinder material mass transport, the permeability (χ) along the *Z*-axis direction was calculated for the separator at the pristine state (Figure 4c, without deposits) and after the 1st cycle (Figure 4f, with deposits). The *Z*-axis is cathode to anode direction. To minimize the computational effort, subvolumes ($275 \times 180 \times 135$ voxels) are cropped in the middle of the entire volume. The streamlines, assigned to multiple colors according to velocity scale, are used for the visual comparison. Correspondingly, the permeability values along three principal directions in the same subdomain are summarized in **Table 2**. Clearly, the permeability of the pristine sample ($\chi_{pristine-z} = 0.13$) is lower than that after one cycle ($\chi_{cycle-z} = 0.21$). Kok et al.[20] proposed that higher permeability of fibrous mats will lead to lower advection and diffusion. Hence, insoluble MgS_x products inevitably block the Mg^{2+} transportation, and decrease the reversibility of sulfur conversion since $\chi_{fresh-z} < \chi_{cycle-z}$. We speculate these deposits will continue to accumulate with increasing cycle numbers. The permeability value along the *X*-axis is much higher than that along the *Y*- and *Z*-axis directions because the flow along the *X*-axis is parallel to the fiber-multilayer.

Table 1. The quantification of morphological parameters extracted from the entire super-P coated separator at different lifecycles.

Cycle number	Phase volume fraction [%]			Surface area per volume [μm² μm⁻³]		
	Air/carbon	Fiber	Deposition	Air/carbon	Fiber	Deposition
0	85.01	14.99	0	0.26	1.61	0
1	72.82	14.08	13.10	0.89	2.08	1.82

Table 2. The permeabilities of liquid electrolyte flow within subvolumetric separator at principal directions (*X*-, *Y*-, and *Z*-axis) before (without depositions) and after 1st cycled (with depositions). It should be noted that the *Z*-axis is aligned with the anode, separator, and cathode (electric current flow direction).

Cycle no.	Permeability [μm²]		
	X-axis	*Y*-axis	*Z*-axis
0	0.98	0.25	0.13
1	0.84	0.21	0.21

**ADVANCED
SCIENCE NEWS**
www.advancedsciencenews.com

**small
methods**
www.small-methods.com

In fact, this approach can be applied in other metal–sulfur systems to evaluate the active materials loss against the states of charge and cycle number. This will rely on the availability of operando datasets which usually establish the permeability as a function of cycling state in real-time.

The charge-state S/C cathode microstructures, at (a–c) pristine and (d–f) 1st, (g–i) 3rd, and (j–l) 10th cycle, are measured by nano-CT in **Figure 5** and Movies S2–S5 (Supporting Information). The active phases (sulfur) are then quantified as they mainly determine the sulfur-based cell performance,[21] such
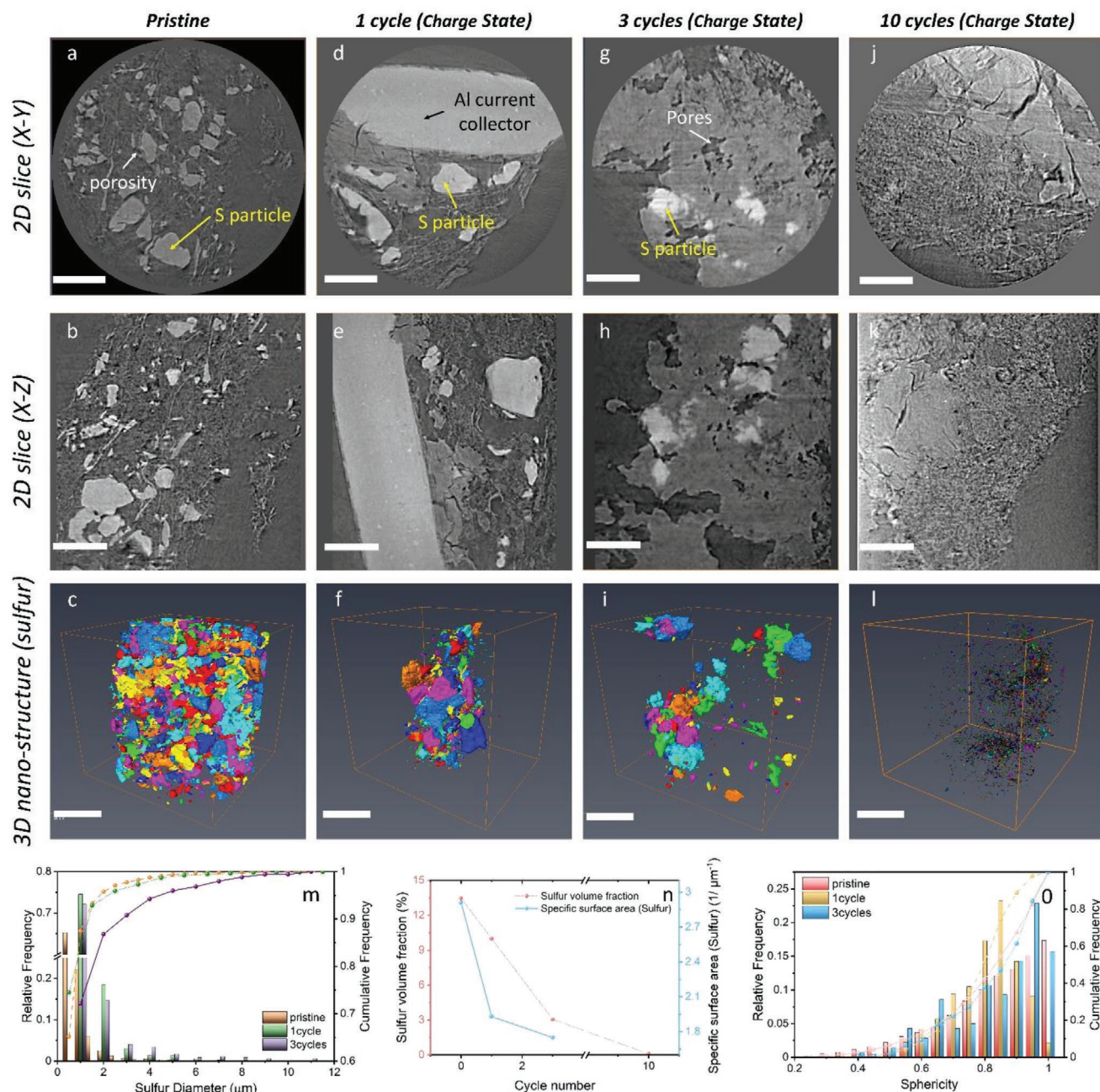

Figure 5. The Zernike phase-contrast nano-CT image of a–c) the pristine, d–f) 1st cycle, g–i) 3rd cycles, and k–l) 10th cycles of carbon–sulfur (S/C) cathode in the Mg/S battery. The orthogonal slice of X–Y plane (a,d,g,j) and X–Z plane (b,e,h,k) of the S/C cathode. The highly attenuating phase near Al current collector in the cycled cathodes suggests the significant densification of carbon binder domain (CBD). Correspondingly, 3D nano-CT images of the individual sulfur particles (with each particle assigned a different color to its neighboring particle) at the pristine (c), 1st (f), 3rd (i), and 10th cycled (l) show significant reduction of sulfur particles. The associated quantification (raw four) of m) particle diameter, n) volume and surface area, and o) sphericity are also demonstrated, indicating the S particle agglomeration and spheroidization after 3 cycles. The ex situ nanostructures highlight the cycled-induced structural degradation process at S/C cathode, including the active sulfur loss, reduction of porosity, and densification of CBD phase. The scale bars represent 20 μm for all figures.

as rate capability. In the 3D renderings, both carbon binder domain (CBD) and porosity phase are deliberately removed in order to present the sulfur particles more clearly. It is should be noted that the nano-CT resolution (≈126 nm) cannot resolve the smallest nanopores; whilst the CBD morphology is different for each battery chemistry, elsewhere these have been reported to have an average diameter of ≈60 nm.[22] However, the sub-micrometer (>150 nm) and micrometer (>400 nm) pores can be resolved comfortably by this technique.

In Figure 5a,b, for the pristine cathode, the 2D slices show the sulfur particles (highly attenuating dense particles), and CBD mixed with porosity (lowest attenuation value). After the 1st cycle, we observed plenty sulfur particles (diameter is up to ≈20 μm) are still able to be converted from MgS_x upon charging (Figure 5d,e). Also, it is interesting to find that the CBD phase is likely to be densified near the Al current collector, and similar phenomena is repeated in 10th cyclic sample (Figure 5j,k). In Figure 5g,h, after 3rd cycle, the sulfur number significantly reduced (the corresponding histogram in Figure S3 of the Supporting Information shows the S counts dropped after cycling), and a complete densification of the CBD within the cathode has occurred, which is also represented by the change of X-ray grayscale. In addition, we observed that the sub-micrometer pores (Figure 4a,b) within the CBD were agglomerated in subsequent cycling, leading to formation of micro- or mesopores (Figure 5d,e,g,h). The X-ray histogram (Figure S3, Supporting Information) shows obvious peak at lower grayscale values because the porosity becomes consolidated and pores are produced. This can also be validated by quantifying the specific surface area of porosity ($S_{Area-porosity}$), which decreases from 5.43 (pristine) to 2.06 μm² μm⁻³ (after 3rd cycle). The aforementioned reaction mechanism of Mg/S cell at the S/C cathode involves solid–liquid–solid transformation during a discharge-charge procedure. Also, its final product of MgS is a nanocrystalline phase[10] that cannot fully convert into elemental S_8 by charging. Hence, it is possible for them to diffuse back to cathode (via the shuttle effect) and fill the smallest pores, thus leading to the CBD densification. These particles in the 3rd and 10th cycled cathodes could be a mixture of S, MgS_2, and MgS. The quantification of all phases within the entire cathode at the pristine and cycled state are summarized in **Table 3**.

Meanwhile, four successive 3D nano-CT images of sulfur particles before (Figure 5c; Movie S2, Supporting Information) and after various cycle numbers (Figure 5f,i,l; Movies S3–S5, Supporting Information) demonstrate a great reduction of active materials. Indeed, the S quantification validates 3D observations. In Figure 5n, the sulfur volume fraction ($V_{f-sulfur}$) decreases from 13.5% at pristine state, to 10% after 1st cycle, then it undergoes a further reduction to 3% after 3rd

cycle. Finally, the sulfur is almost consumed (only 0.7% after 10th cycle). Such reduction of active materials is likely attributed to the formation of insoluble phases (transformation from elemental S_8 to MgS_x and/or MgS[4]). The $S_{Area-sulfur}$ decreases from 2.91 (pristine) to 1.74 μm² μm⁻³ (3rd cycle) due to the re-appearance of sulfur particles with larger diameter and some smaller S particles dissolution. We used the particle size distribution (PSD) to study the effect of cycle number on active particle by quantifying the equivalent spherical diameter of each S particles (Figure 5m). Uncycled sulfur particles, range between 500 nm and 4.5 μm, are nearly homogenously distributed within the field of view (FoV), and ≈90% of particle diameter is smaller than 1 μm. However, the PSD of 3rd cycled sulfur is in the range between 1 and 11.5 μm, and ≈15% of particles are larger than 2 μm diameter, suggesting significant agglomeration of sulfur. Such behavior, in a similar manner to Li/S cells, is largely due to the reaction of the cathode and electrolyte. Figure 5o shows the distribution of sphericity (Ψ) of sulfur particles (Ψ is defined as $\Psi = (\pi^{1/3} * 6 U^{2/3})/A$, where U is the particle volume and A its surface area, Ψ = 1 means that the particle is perfectly spherical). Generally, the cycled sulfur (Figure 5g–i) has greater sphericity than those uncycled S particles where stripe-like and droplet-like sulfur particles are seen in Figure 5a,b. We did not quantify the 10th cycled sulfur because their sizes are usually smaller than 10 voxels which is not comparable with others.

Direct (cathode) and indirect (separator) evidence of sulfur loss are demonstrated in Figures 5 and 4, respectively. Correlative X-ray imaging studies reveal that the polysulfide shuttle effect,[23] which is widely acknowledged in Li–S cells, is also inevitable in the Mg/S cell. We propose that the pore agglomeration, and active material (sulfur) dissolution occurs as a result of cathode degradation via a similar mechanisms to those reported for Li/S batteries.[24]

2.2. Simulation on Effective Diffusivity on the Electrode and Its Metrics

A grayscale sensitivity analysis was performed on the nano-CT data of the pristine S/C cathode (Figure 5). We aimed first to determine the accurate grayscale value of porosity, and then study the effect of manual segmentation on cell metrics (i.e., the tortuosity). The cropped S/C image (grayscales vary between 0 and 65535 for the 16-bit image) is shown in **Figure 6**a. Histogram analysis (Figure S2, Supporting Information) shows that three-phase segmentation could be identified. The threshold for sulfur phase is above ≈32 500, while the pore threshold is below ≈23 100. Hence, some uncertainties exist in segmenting the interfacial regions between CBD and pores, because voxels at the boundaries between CBD and pores may belong to more than a single phase (the partial volume effect).[25] Recent studies[26] have demonstrated the use of machine-learning-assisted approaches to address the threshold uncertainty in LIBs, for instance, by adding an error bar to the models.[26b] We ascertain the pore threshold by manually segmenting five different grayscale values range from 21 900 (Figure 6b) to 23 100 (Figure 6c) with a step of 300. The results show that the porosity (ε), the effective diffusivity (D_{eff}), the tortuosity (τ), and the surface area

Table 3. The quantification of morphological parameters within the entire S/C electrode at different stages in cell developmental lifecycle.

Cycle no.	Phase volume fraction [%]		Surface area per volume [μm² μm⁻³]	
	Porosity	CBD	Porosity	CBD
0	31	55	5.43	4.38
1	28	62	4.37	5.68
3	30	66	2.06	1.13

**ADVANCED
SCIENCE NEWS**

www.advancedsciencenews.com
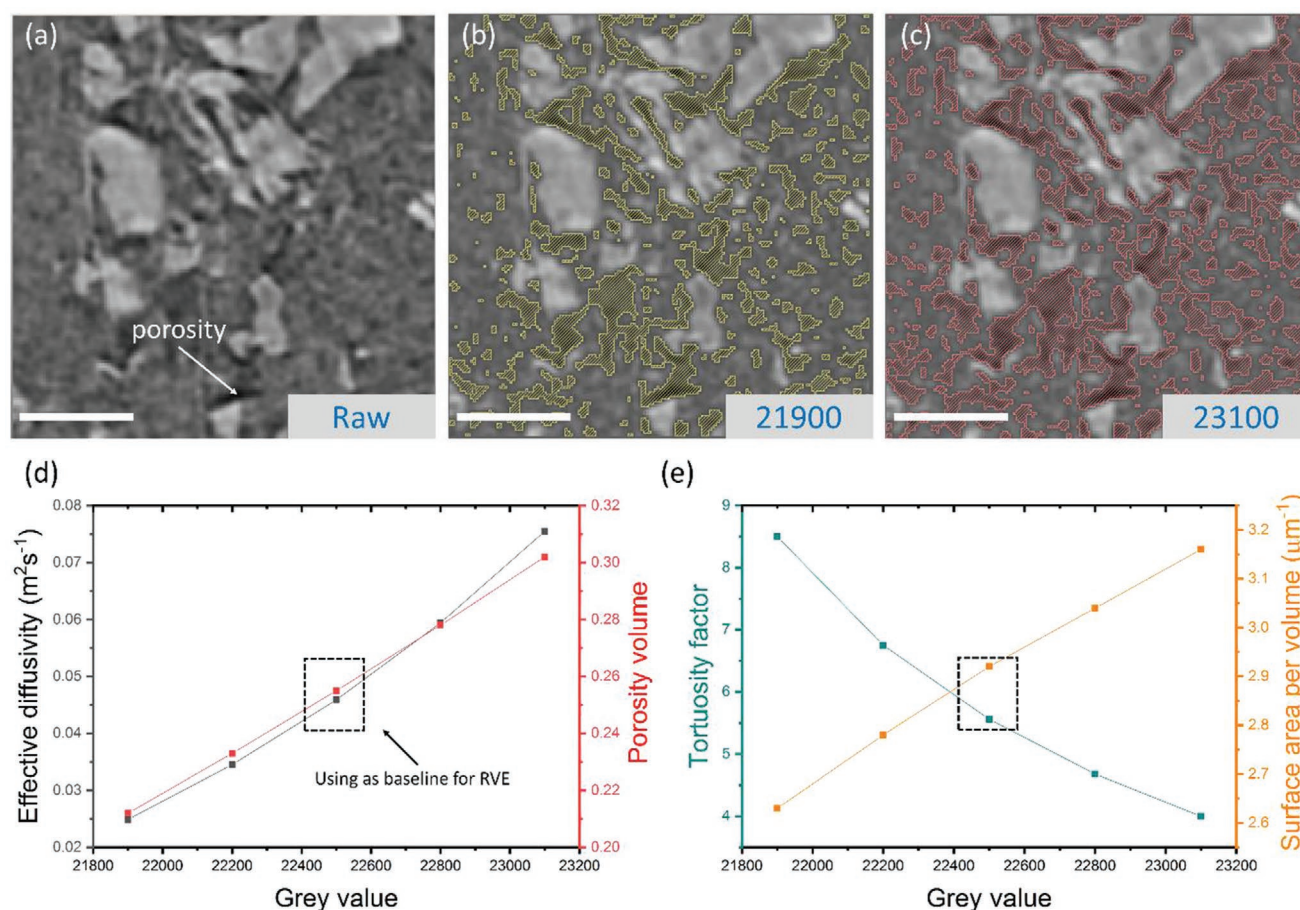
**small
methods**

www.small-methods.com

Figure 6. a) 2D orthogonal slice is extracted from reconstructed volume of pristine cathode, and an unsharp masked filter was applied. Two grayscale values of b) 21 900 and c) 23100 were used to segment porosities for the same slice, respectively. The variation in d) the effective diffusivity and the porosity, and e) the tortuosity factor and the surface area per volume according to progressively chosen grayscale value (from 21 900 to 23 100 as an interval step of 300) are calculated in TauFactor at the X-axis direction, indicating the effect of threshold selecting on the real battery transport evaluation. The increased grayscale value leads to the higher porosity volume and surface area but lower tortuosity. The mediate value of 22 500 is used as best segmentation baseline of pore phase for further RVE studies (Figure 7). All scale bars represent the 5 µm.

(S_{Area}) range from 21–30%, 0.25–0.75 m² s⁻¹, 4.0–8.5, and 2.62–3.15 µm² µm⁻³. In Figure 6d,e, assigning a higher grayscale number will increase the D_{eff}, ε, and S_{Area} values but decrease the τ value. Hence, the selection of this value has a considerable effect on its physical quantities. Through this attempt, the intermediate value of 22 500 was chosen for pores as a baseline for further representative volume element (RVE) investigation as it represents the best segmentation. An SEM of the same cathode is presented in Figure S3 of the Supporting Information to support the selection of pore threshold. The porosity fraction obtained by SEM (≈26%) is comparable to that by nano-CT (28–31%). In spite of the uncertainty of estimating the size of nanopores, the measurement is therefore believed to be reliable for other materials in the system.

The tortuosity (τ) values are plotted against fraction of total volume (**Figure 7**g–i) according to five RVE analyses. It is found that $\tau_{(X\text{-axis})}$ (Figure 7g) are close to $\tau_{(Z\text{-axis})}$ (Figure 7i). However, $\tau_{(Y\text{-axis})}$ (Figure 7h) is much larger than values in the X- and Y- directions when the smaller volumes (i.e., sample 1 and 2) are selected. Moreover, both $\tau_{(sample\ 4)}$ and $\tau_{(sample\ 5)}$ show minor fluctuations regardless of the principal directions considered when

the volume fraction increases from 0% to 100%, indicating that the RVE criteria has been satisfied. The triple phase boundary (TPB) of S/C cathode fluctuated between 1.23 (sample 1) and 1.41 (sample 5) µm⁻². The TPBs were fitted using linear approximation (Figure 7k), and oscillation in value was dampened when a selected volume over the RVE was analyzed. The effect of RVE on both V_f and S_{Area} are then reported in Figure 7l,m. The result shows that the $V_{f\text{-sulfur(local)}}$ and $S_{Area\text{-sulfur(local)}}$ at local regions are obviously varied from that result from the bulk sample (Table 3), demonstrating the importance of selecting an appropriate RVE for local electrode measurements. The representative volume for this S/C cathode is suggested to be larger than ≈8200 µm³ (sample 4, 160³ voxels).

2D-projected mass flux demonstrates completely different pathways for the pristine (Figure 7a) and the 3rd cycled (**Figure 8**d) electrode as high flux region is homogeneously distributed for pristine sample. The brighter colors represent high-flux density regions while the darker area indicates low-flux density. 3D flux distributions are correspondingly rendered in Figure 8b,e. Both $X+$ and $X–$ axis are assumed to be in and out diffusive direction, respectively. Clearly, a number
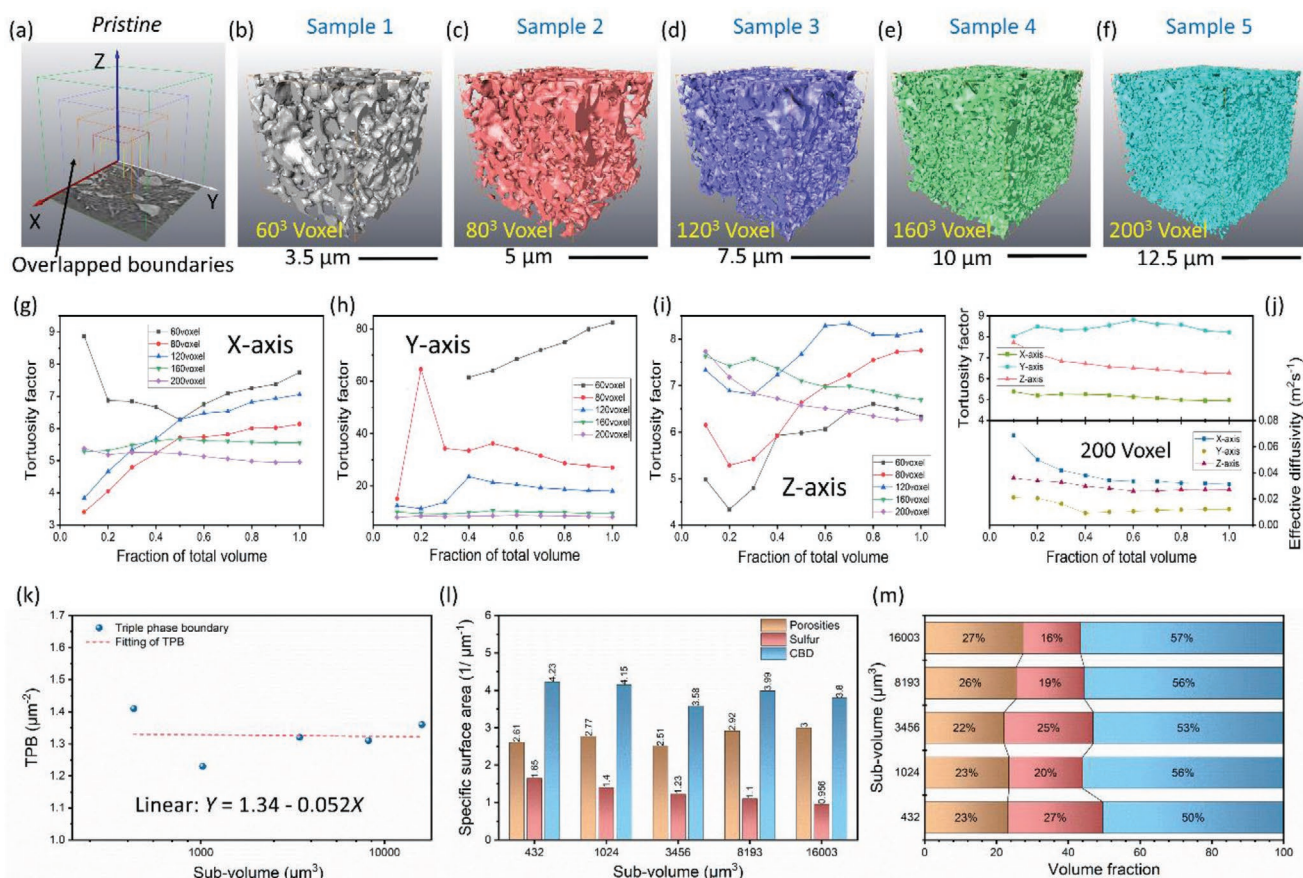
Figure 7. a) The progressively increased cubic volumes (from 60^3 to 200^3 voxels, termed as sample 1 to sample 5) are selected to study the effect of representative volume element (RVE) on tortuosity and porosity (based on TauFactor simulation). b–f) Associated porosity within the pristine S/C cathode are rendered in different colors, which represent various subvolumes from 432 to 16 003 μm^3. g–i) The relationship between the fraction of total volume and tortuosity factor at X-, Y-, and Z-axis directions, respectively. j) The comparative study of tortuosity against diffusivity at three-plane by using the fixed subvolume of 16 003 μm^3. k) The triple phase boundary (TPB) results within various subvolumes and linear fitting. The effect of the RVE on l) the specific surface area and m) volume fraction.

of thinner streamlines show homogenous channels with higher flux, which can facilitate the diffusion at the pristine state (Figure 8b). By contrast, the diffusion and related material transportation could be restricted after the cycles since the flux gradually decreased (Figure 8e). Moreover, 3D pore networks before (Figure 8c) and after (Figure 8f) cycling are rendered (both sulfur and CBD phases are not shown), showing that the local porosity (ε_{local}) for pristine and three cycled samples are 22% and 10%. The cycled sample with a lower porosity is expected to have a consequent decrease in the percolation of the pore-network.

Again, 3D imaging provides additional insight into the cell degradation, and could be considered as an approach to directly evaluate the Mg/S performance by visualizing "bottle-necks" of diffusive channels as the pore-network has a major influence on the mass transport pathways and ion-conductivity during cycling.

2.3. The Electrochemical Performance

In **Figure 9**a, the cyclic voltammetry (CV) of Mg/S cell containing a super-P functional layer at a scan rate of 0.03 mV s^{-1}

is presented. The cathodic peak is located at ≈1.01 V corresponding to the reduction reaction of S_8 to magnesium polysulfides (MgS_x) and then to MgS, respectively. In the subsequent anodic process, the oxidation peak is observed at ≈2.05 V, which relates to the reverse reaction of MgS to long-chain polysulfides (MgS_x), then to S.

The voltage–capacity curves demonstrate the good reversibility after 3 cycles at 0.03 C (Figure 9b). The discharge reversible capacity of 772 mAh g^{-1} is achieved in the 1st cycle, and this is ≈46% of the theoretical gravimetric specific capacity of sulfur at 1672 mAh g^{-1}. In Figure 9c, the Mg/S cell with super-P layer has higher capacity during 15 cycle life than that used traditional separator, and thus the capacity decay ratio of super-P modified separator (5.0% ratio) is lower than traditional separator (5.6% ratio). Such capacity retention is attributed to the good electric conductivity in both the composite sulfur cathode and coated separator, which decreases the interface resistance between the cathode and separator. The super-P carbon is unlikely to react with Mg anode as validated in Figure S5 of the Supporting Information. The discharge plateaus are at ≈1.1 V, and the related charge plateaus at ≈2.1 V, which are in good agreement with the CV measurement (Figure 9a). The
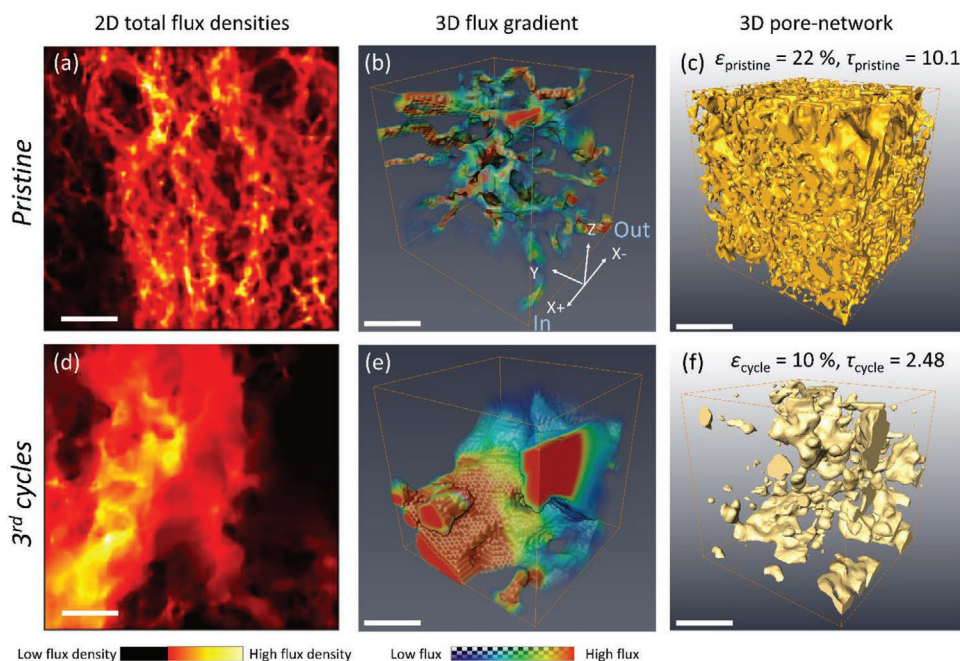
Figure 8. The total flux within a) the pristine and d) the 3rd cycled electrodes at *X*-axis calculated from the TauFactor. 3D flux distribution in b) the pristine and e) the 3rd cycled electrodes based on effective diffusivity simulations are rendered. The comparison of pore networks of 3D microstructures c) before (local porosity, $\varepsilon_{pristine} = 22\%$) and f) after cycling ($\varepsilon_{cycle} = 10\%$). The microstructure size in (c) and (f) is $120 \times 120 \times 120$ voxels, and all scale bars represent the 7.5 µm.
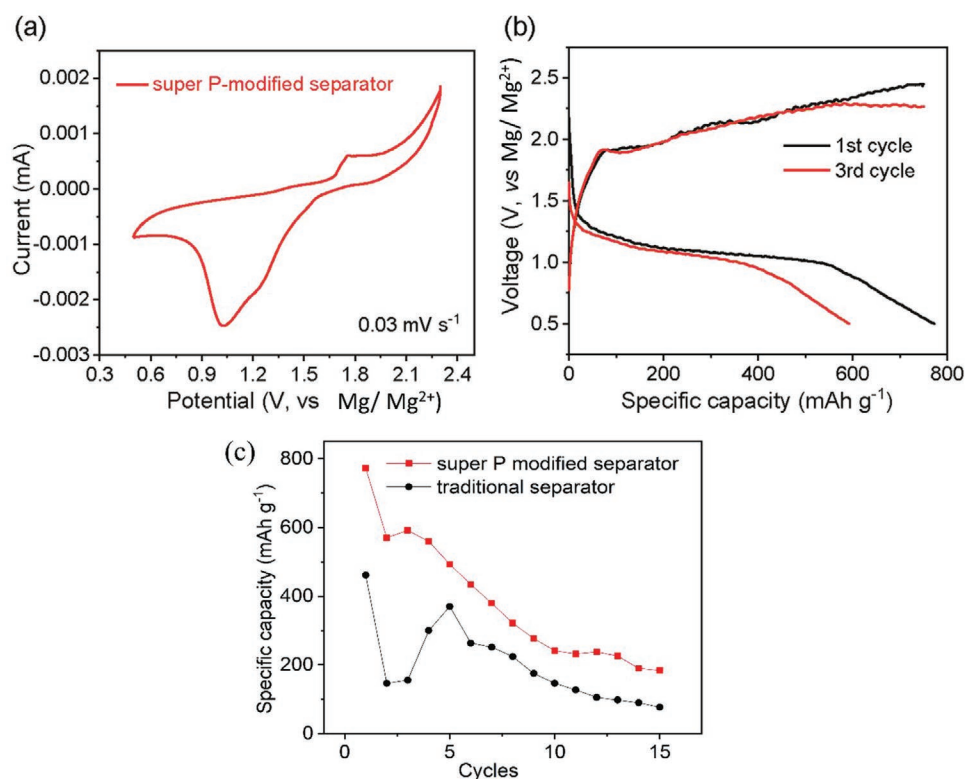

Figure 9. a) The cyclic voltammetry (CV) of Mg/S cell with super-P functional layer at the scan rate of 0.03 mV s^{-1}. b) The charge/discharge profile of electrochemical cell after the 1st and 3rd cycle at the 0.03 C-rate. c) The cycling performance of Mg/S cell without and with super-P layer for 15 cycles at same C-rate. The functional separators were imaged at microscale before and 1 cycle, while the S/C cathodes were scanned at nanoscale before and after 1st, 3rd, and 10th cycle.

**ADVANCED
SCIENCE NEWS**
www.advancedsciencenews.com

**small
methods**
www.small-methods.com

reduction in specific capacity in the Mg/S cell during cycling is attributed to the microstructure degradation (i.e., dissolution of sulfur particles and pore agglomeration at cathode side) which was discussed above sections. The X-ray tomography help to advance the development of S/C cathode, revealing, for example, the relationship between active S particle size and its performance in Li/S cells (the rate capability and capacity retention upon cycling).[21]

3. Conclusion

High-resolution, nano-CT provides an opportunity to observe the structural evolution of S/C cathode and correlate with electrochemical performance. It provides a route for quantifying microstructural parameters including the volume fraction, specific surface area, particle size distribution, tortuosity, etc. It has highlighted the sulfur dissolution, the CBD densification and porosity agglomeration over early life cycling, which are thought to be mainly responsible for the electrode degradation and subsequent cell failure. The RVE for S/C cathode should be larger than ≈ 8200 μm^3 to obtain reliable measurements (i.e., TPB and surface area) that represent bulk materials.

Micro-CT reveals that the insoluble polysulfides were produced upon cycling. This indirectly provides evidence of active materials loss as sulfur dissolves into the electrolyte and reacts with Mg. The higher permeability of the separator after the cycle suggests that the polysulfides decrease the mass transport, thus leading to the performance drop.

The microstructure evolution in the early stages of Mg/S cell cycling highlights the challenges of electrode design, and undoubtedly requires the multiscale and multimodal characterizations to comprehensively understand the electrode behaviors. Future work will be focused on cell development to achieve longer lifespan, and 4D (4D plus time) X-ray imaging investigations will be performed to improve the fundamental understanding of the dynamic degradation mechanisms.

4. Experimental Section

Electrode Preparation, Cell Fabrication, and Electrochemical Cycling: A commercial magnesium foil was used as the anode and an S/C composite as the cathode. The sulfur cathode was prepared by mixing commercial sulfur powder (Sigma, UK), super P, carbon nanotube, graphene, carboxymethyl cellulose (CMC), and styrene-butadiene (SBR) in a weight ratio of 50:20:5:5:10:10 in deionized water. The super P, CMC, and SBR were purchased from MTI Corporation and the carbon nanotube and graphene were purchased from XFNANO. The mixture was then transferred into a batch reactor under argon with subsequent heating. The slurry was coated on an aluminum foil and dried at 80 °C overnight in a vacuum oven. Next, the electrode was punched into 6 mm diameter disks (with mass loading from 0.1–1 mg_{sulfur} cm^{-2}) and its diameter was further reduced to 2.5 mm by low energy and frequency laser beam (Cimita, Oxford Lasers Ltd). The electrolyte consisted of 0.9 M Mg-HMDS in a solution of TEGDME with $AlCl_3$ and $MgCl_2$.[18] The super-P coated separator was also laser machined into a round disc with a diameter of 3 mm. The separator was modified by coating a layer containing super P, CMC, and SBR in a weight ratio of 90:5:5. The ratio of sulfur to electrolyte was 0.1 mg μL^{-1} for all the cells. Finally, all aforementioned components were assembled within a regular 1/8″ PFA Swagelok straight union (PFA-220-6, Swagelok) in an Ar-filled glovebox.

The CV measurements were performed on an electrochemical workstation (Interface 1000E, Gamry Instruments) at a scan rate of 0.03 mV s^{-1} with a voltage range of 0.5–2.3 V at room temperature. All galvanostatic charge and discharge tests were also measured using the electrochemical workstation (Interface 1000E, Gamry Instruments) and the battery measurement system (Neware, China).

After cycling, the PFA Swagelok cells were disassembled in an Ar-filled glovebox and washed by TEGDME solvent, and then the sulfur cathode, super-P modified separator, and Mg anode were harvested and mechanically prepared for characterization. The sulfur electrode samples were prepared under a visible light microscope and mounted onto the tip of stainless-steel needles using epoxy resin. The remaining portions of samples were reserved for SEM. In this study, the voltages of discharge-state and charge-state sample are 0.5 and 2.3 V, respectively.

Scanning Electron Microscopy and Energy Dispersive X-Ray Spectroscopy: Both anode and cathode at the pristine and cycled state were imaged at a working distance of 8 mm using a Zeiss EVO MA10 (Carl Zeiss AG, Germany) scanning electron microscope (SEM). Energy dispersive X-ray spectroscopy (EDX) was subsequently applied for chemical identification using an AztecONE detector (Oxford Instruments, Oxford, UK) with an accelerating voltage of 15 kV and analyzed using the INCA software package.

X-Ray Photoelectron Spectroscopy: XPS analysis was performed using a Kratos Axis SUPRA XPS fitted with a monochromated Al kα X-ray source (1486.7 eV), a spherical sector analyzer and 3 multichannel resistive plate, 128 channel delay line detectors. All data were recorded at 150 W and a spot size of 700×300 μm. Survey scans were recorded at a pass energy of 160 eV, and high-resolution scans recorded at a pass energy of 20 eV. Electronic charge neutralization was achieved using a magnetic immersion lens. Filament current= 0.27 A, charge balance= 3.3 V, filament bias= 3.8 V. All sample data were recorded at a pressure below $10–8$ Torr and a room temperature of 294 K. Electrodes datasets were analyzed using CasaXPS v2.3.20PR1.0 and the spectra were calibrated with C1s peak at 284.8 eV.

Lab-Based X-Ray Micro- and Nanocomputed Tomography: A lab-based X-ray micro-CT instrument (ZEISS Xradia 520 Versa, Carl Zeiss Inc.) was used to collect tomograms of the pristine and cycled super-P separator. A 20× lens was used, and a binning of 1 was set on the 2048×2048 pixels CCD detector to achieve a pixel size of ≈ 390 nm with a field of view of $\approx 750 \times 750$ μm^2. A polychromatic cone-beam source using a tungsten target with the voltage set at 40 kV was used. There is no significant geometric magnification and/or phase contrast effects since the source–sample and sample–detector distances were minimized to maximize intensity. For each set of tomographic data, 1601 projections were obtained with an exposure time of 40 s.

A lab-based X-ray nano-CT instrument (ZEISS Xradia 810 Ultra, Carl Zeiss Inc.) was used to image the fresh and cycled S/C cathodes. The X-rays are generated from a rotating Cr source producing a quasi-monochromatic X-ray beam with a Cr characteristic emission peak of 5.4 keV. An optional Au ring inside the optics chamber was used to achieve Zernike phase contrast imaging.[12b] This technique allows to resolve the CBD pore morphology (Figure S4, Supporting Information). A capillary condenser produces focused X-rays for a full-field illumination of the sample which is projected onto the 1024×1024 pixels CCD detector using a Fresnel zone plate. A large field of view mode with a binning pixel size of 2 was used, resulting in an FOV of 64×64 μm with a pixel size of 126 nm. The sample was continually rotated from 0° to 180° and a total of 1601 projections were taken with 32 s exposure time. The details of the micro- and nano-X-ray imaging parameters for each sample are presented in **Table 4**.

Imaging Processing, Data Analysis, and Image-Based Modeling: Both micro- and nanoradiographic projections were reconstructed using a filtered-back projection algorithm (XMReconstructor, Carl Zeiss Inc.). Both reconstructed micro-CT and nano-CT datasets were imported into Avizo 2019.4 (ThermoFisher) for further segmentation and quantification. An unsharp masking filter was applied to sharpen the edge of sulfur particles and fibers without increasing the noise.

Table 4. The micro- and nano-X-ray tomographic imaging acquisition parameters.

Sample	Scan type	Photon energy [keV]	FOV [µm²]	Detector binning	Exp time [s]	Projection no.	Cyclic status
Super-P separator	Micro-CT	40	750 × 750	1	40	1601	Fresh
Super-P separator	Micro-CT	40	750 × 750	1	40	1601	1 cycle
S/C electrode	Nano-CT	5.4	64 × 64	2	32	1601	Fresh
S/C electrode	Nano-CT	5.4	64 × 64	2	32	1601	1 cycle
S/C electrode	Nano-CT	5.4	64 × 64	2	32	1601	3 cycles
S/C electrode	Nano-CT	5.4	64 × 64	2	32	1601	10 cycles

The pristine and charge-state cycled cathodes, imaged by nano-CT, were then segmented (based on grayscale values) into three phases consisting of sulfur, CBD, and pores. The sulfur phase was then separated into individual particles and, the label analysis was performed on these separated S particles in Avizo, revealing the metrics of the electrode (i.e., average particle size and sphericity).

The electrolyte flow within separators was simulated by applying the commercial computational software Avizo XLab (an image-based model based on the Stokes' equations) to determine the permeability in the Mg/S system. The relative velocity of flow was simulated in three directions along the *X*-, *Y*-, and *Z*-axis using tomography data before and after the 1st cycle. The assumptions and the boundary conditions for modeling were as follows: a low Reynolds number velocity inlet (Re < 0.1) since the electrolyte volume is very low and has high viscosity, no volume changes during cycling and, the inlet (cathode side) and outlet (anode side) pressures are fixed after cycling. The input and output pressures were set as 130 and 100 kPa, respectively. No-slip conditions were applied on four outer walls, and no-slip conditions on the interior walls representing solid–liquid interfaces. The electrolyte composition remains unchanged and its viscosity was set to be the same before and after cycle (0.001 Pa s).

The RVE Analysis: Five subvolumes were extracted, and the microstructural parameters (such as tortuosity) of the pore phase were then determined by using Matlab 2019 with the TauFactor plugin.[27] The RVEs were implemented to determine the relationship between the local tortuosity (τ_{local}) and the local effective diffusivity ($D_{eff\text{-}local}$). The overlapped boundaries (Figure 7a) of five cubic sub-volumes (60^3, 80^3, 120^3, 160^3, and 200^3 voxels) were progressively extracted within the entire S/C electrode at fresh state. Correspondingly, their subvolumes range from 432 to 16003 µm³ referred to as sample 1 to sample 5. The same threshold of porosity is applied to all cases, and the associated segmentations were rendered in Figure 7b–f. The largest volume is sample 5 which is nearly 37 times larger than sample 1, allowing us to identify the RVE effect. Moreover, the TauFactor software can provide the fluxes for the S/C cathode before and after three cycles along the *X*-axis direction.[27]

Supporting Information

Supporting Information is available from the Wiley Online Library or from the author.

Conflict of Interest

The authors declare no conflict of interest.

Data Availability Statement

The data is available for reasonable request.

[1] a) M. Wild, L. O'Neill, T. Zhang, R. Purkayastha, G. Minton, M. Marinescu, G. J. Offer, *Energy Environ. Sci.* **2015**, *8*, 3477; b) A. Manthiram, Y. Fu, S.-H. Chung, C. Zu, Y.-S. Su, *Chem. Rev.* **2014**, *114*, 11751; c) X. Ji, K. T. Lee, L. F. Nazar, *Nat. Mater.* **2009**, *8*, 500; d) A. Manthiram, S. H. Chung, C. Zu, *Adv. Mater.* **2015**, *27*, 1980; e) L. Carbone, S. G. Greenbaum, J. Hassoun, *Sustainable Energy Fuels* **2017**, *1*, 228; f) J. Tan, D. Liu, X. Xu, L. Mai, *Nanoscale* **2017**, *9*, 19001.

[2] V. Marangon, D. Di Lecce, F. Orsatti, D. J. Brett, P. R. Shearing, J. Hassoun, *Sustainable Energy Fuels* **2020**, *4*, 2907.

[3] B. P. Vinayan, Z. Zhao-Karger, T. Diemant, V. S. Chakravadhanula, N. I. Schwarzburger, M. A. Cambaz, R. J. Behm, C. Kubel, M. Fichtner, *Nanoscale* **2016**, *8*, 3296.

[4] P. Wang, M. R. Buchmeiser, *Adv. Funct. Mater.* **2019**, 29.

[5] L. Kong, C. Yan, J. Q. Huang, M. Q. Zhao, M. M. Titirici, R. Xiang, Q. Zhang, *Energy Environ. Mater.* **2018**, *1*, 100.

[6] S. H. Chung, A. Manthiram, *Adv. Mater.* **2019**, *31*, 1901125.

[7] Z. Zhao-Karger, R. Liu, W. Dai, Z. Li, T. Diemant, B. Vinayan, C. Bonatto Minella, X. Yu, A. Manthiram, R. J. r. Behm, *ACS Energy Lett.* **2018**, *3*, 2005.

[8] A. Du, Y. Zhao, Z. Zhang, S. Dong, Z. Cui, K. Tang, C. Lu, P. Han, X. Zhou, G. Cui, *Energy Storage Mater.* **2020**, *26*, 23.

[9] L. Yin, H. Dou, A. Wang, G. Xu, P. Nie, Z. Chang, X. Zhang, *New J. Chem.* **2018**, *42*, 1431.

[10] B. P. Vinayan, H. Euchner, Z. Zhao-Karger, M. A. Cambaz, Z. Li, T. Diemant, R. J. Behm, A. Gross, M. Fichtner, *J. Mater. Chem. A* **2019**, *7*, 25490.

**ADVANCED
SCIENCE NEWS**

www.advancedsciencenews.com

**small
methods**

www.small-methods.com

[11] L. Sheng, Z. Hao, J. Feng, W. Du, M. Gong, L. Kang, P. R. Shearing, D. J. Brett, Y. Huang, F. R. Wang, *Nano Energy* **2021**, *83*, 105832.

[12] a) P. Pietsch, V. Wood, *Annu. Rev. Mater. Res.* **2017**, *47*, 451; b) M. Endrizzi, *Nucl. Instrum. Methods Phys. Res., Sect. A* **2018**, *878*, 88; c) T. M. M. Heenan, C. Tan, J. Hack, D. J. L. Brett, P. R. Shearing, *Mater. Today* **2019**, *31*, 69; d) S. R. Daemi, X. Lu, D. Sykes, J. Behnsen, C. Tan, A. Palacios-Padros, J. Cookson, E. Petrucco, P. J. Withers, D. J. L. Brett, P. R. Shearing, *Mater. Horiz.* **2019**, *6*, 612.

[13] X. Lu, A. Bertei, D. P. Finegan, C. Tan, S. R. Daemi, J. S. Weaving, K. B. O'Regan, T. M. Heenan, G. Hinds, E. Kendrick, *Nat. Commun.* **2020**, *11*, 2079.

[14] C. Tan, T. M. Heenan, R. F. Ziesche, S. R. Daemi, J. Hack, M. Maier, S. Marathe, C. Rau, D. J. Brett, P. R. Shearing, *ACS Appl. Energy Mater.* **2018**, *1*, 5090.

[15] V. Neburchilov, J. Zhang, *Metal–Air and Metal–Sulfur Batteries: Fundamentals and Applications*, CRC Press, Boca Raton, Florida **2016**.

[16] X.-C. Hu, Y. Shi, S.-Y. Lang, X. Zhang, L. Gu, Y.-G. Guo, R. Wen, L.-J. Wan, *Nano Energy* **2018**, *49*, 453.

[17] J. Häcker, C. Danner, B. Sievert, I. Biswas, Z. Zhao-Karger, N. Wagner, K. A. Friedrich, *Electrochim. Acta* **2020**, *338*, 135787.

[18] Z. Zhao-Karger, X. Zhao, D. Wang, T. Diemant, R. J. Behm, M. Fichtner, *Adv. Energy Mater.* **2015**, *5*, 1401155.

[19] P. Wang, M. R. Buchmeiser, *Adv. Funct. Mater.* **2019**, *29*, 1905248.

[20] M. D. Kok, R. Jervis, T. G. Tranter, M. A. Sadeghi, D. J. Brett, P. R. Shearing, J. T. Gostick, *Chem. Eng. Sci.* **2019**, *196*, 104.

[21] D. Di Lecce, V. Marangon, W. Du, D. J. Brett, P. R. Shearing, J. Hassoun, *J. Power Sources* **2020**, *472*, 228424.

[22] L. Zielke, T. Hutzenlaub, D. R. Wheeler, C. W. Chao, I. Manke, A. Hilger, N. Paust, R. Zengerle, S. Thiele, *Adv. Energy Mater.* **2015**, *5*, 1401612.

[23] M. Wild, G. J. Offer, *Lithium-Sulfur Batteries*, Wiley, Weinheim **2019**.

[24] A. Yermukhambetova, C. Tan, S. R. Daemi, Z. Bakenov, J. A. Darr, D. J. Brett, P. R. Shearing, *Sci. Rep.* **2016**, *6*, 35291.

[25] S. R. Daemi, C. Tan, T. Volkenandt, S. J. Cooper, A. Palacios-Padros, J. Cookson, D. J. L. Brett, P. R. Shearing, *ACS Appl. Energy Mater.* **2018**, *1*, 3702.

[26] a) Z. Jiang, J. Li, Y. Yang, L. Mu, C. Wei, X. Yu, P. Pianetta, K. Zhao, P. Cloetens, F. Lin, *Nat. Commun.* **2020**, *11*, 2310; b) C. Martinez, K. M. Potter, M. D. Smith, S. A. Roberts, *Volumetric Anomaly Detection in X-ray CT Scans through Uncertainty Quantification*, Albuquerque, NM, USA **2019**.

[27] S. J. Cooper, D. S. Eastwood, J. Gelb, G. Damblanc, D. J. L. Brett, R. S. Bradley, P. J. Withers, P. D. Lee, A. J. Marquis, N. P. Brandon, P. R. Shearing, *J. Power Sources* **2014**, *247*, 1033.